

Isospin Projected Antisymmetrized Molecular Dynamics and its Application to ^{10}B

Hiroyuki Morita¹ and Yoshiko Kanada-En'yo¹

¹*Department of Physics, Kyoto University, Kyoto 606-8502, Japan.*

**E-mail: morita.hiroyuki.47a@st.kyoto-u.ac.jp*

.....
 To investigate pn pair correlations in $N = Z = \text{odd}$ nuclei, we develop a new framework based on the generator coordinate method of the $\beta\gamma$ constraint antisymmetrized molecular dynamics. In the framework, the isospin projection is performed before the energy variation to obtain the wave function optimized for each isospin. We apply the method to ^{10}B and show that it works well to describe coexistence of $T = 0$ and $T = 1$ states in low-energy spectra. Structures of low-lying states and pn correlations are investigated. Strong $M1(0_1^+ \rightarrow 1_1^+)$ and $E2(1_1^+ \rightarrow 1_2^+)$ transitions are understood by the spin excitation of the pn pair and the rotation of a deformed core, respectively.

.....
 Subject Index D11

1 Introduction

Proton and neutron (pn) correlation is one of the key phenomena to understand properties of nuclei along the $N = Z$ line in the nuclear chart (see Ref. [1] and references therein). Unlike in identical pair correlations, two channels, $T = 0$ and $T = 1$, are possible in pn pair correlations, and both channels play an important role in various nuclear structures. Competition between $T = 0$ and $T = 1$ pn pairs has been attracting a great interest and discussed to describe level ordering of $J^\pi T = 1^+0$ and $J^\pi T = 0^+1$ states in $N = Z = \text{odd}$ nuclei and neighboring nuclei. In the heavy-mass region, the competition has been investigated with mean-field approaches [2–7]. In the light-mass region, properties of a pn pair at the nuclear surface have been studied in detail to understand low-lying spectra of $N = Z = \text{odd}$ nuclei [8–10].

As discussed in the study with a three-body model calculation [8], a proton and a neutron around a core nucleus form a pn pair in the $T = 0$ or $T = 1$ channel because of the S -wave attraction between nucleons. The $T = 1$ pn pair is the mirror state of the dineutron pair, which is often discussed in neutron-rich nuclei. The appearance of the $T = 0$ pn pair is peculiar to $N = Z = \text{odd}$ nuclei. Unlike the $T = 1$ pair, the $T = 0$ pn pair has the finite intrinsic spin $S = 1$ like a deuteron, and therefore it provides different J states in low-energy region because of angular momentum coupling. Indeed, it is experimentally known that many $T = 0$ states coexist along with the $J^\pi T = 0^+1$ state in low-energy spectra of $N = Z = \text{odd}$ nuclei [1]. Moreover, a high J state with $T = 0$ comes down to the ground state in many $N = Z = \text{odd}$ nuclei in the light-mass region except for those with closed-shell cores. For example, the ground state spin parity of ^{10}B with $Z = N = 5$ is 3^+ , for which the importance of three-nucleon forces is discussed in the no-core shell model calculations [11, 12].

In systematic study of general $N = Z = \text{odd}$ nuclei, it is important to describe the competition between the $T = 0$ and $T = 1$ pn correlations while taking into account spin configurations as well as nuclear deformation. In the light-mass $N = Z$ region, cluster structure is another important feature which brings rich structures together with the pn correlations. The pn pair feature and its dynamics can be affected by the cluster structure.

To deal with these problems, we developed a new method based on the antisymmetrized molecular dynamics (AMD)[13–17] with constraint on quadrupole deformation parameters called $\beta\gamma$ constraint AMD [18, 19]. The $\beta\gamma$ constraint AMD has been proved to be a useful approach to study structures of stable and unstable nuclei. In the AMD method, existence of a core nucleus, a pn pair, and a cluster structure are not *a priori* assumed, but degrees of freedom of all nucleons are independently treated in basis wave functions given by Slater

determinants of Gaussian wave packets. Nevertheless, if a system favors a structure with a pn pair and cluster structures, such the structure is obtained in the energy variation. In the new method, the isospin projection is performed before the energy variation to obtain the AMD wave function optimized for each isospin state. We call this method, the isospin projected $\beta\gamma$ constraint AMD, $T\beta\gamma$ -AMD. Energy levels of $N = Z = \text{odd}$ nuclei are calculated with the $T\beta\gamma$ -AMD method combined with the generator coordinate method (GCM), called $T\beta\gamma$ -AMD+GCM. To test the applicability of the new framework, we apply the method to ^{10}B , in which $2\alpha + pn$ structures are found in low-lying $T = 0$ and $T = 1$ states. We investigate pn correlations around the 2α core, and show the importance of the finite spin of the $T = 0$ pn pair, which couples with the pn motion and the core rotation, in the low-lying states of ^{10}B .

The paper is organized as follows. We explain the framework of the $T\beta\gamma$ -AMD in the section 2, and the adopted effective nuclear interactions in section 3. We show the calculated results of ^{10}B in section 4, and give discussion of structures of ^{10}B focusing on the pn correlation in section 5. Finally, a summary and an outlook are given in section 6.

2 Framework of $T\beta\gamma$ constraint AMD

The antisymmetrized molecular dynamics is one of the useful approaches to describe the cluster aspect of light nuclei. However, the conventional AMD method is not sufficient for $N = Z = \text{odd}$ nuclei, in which the isospin $T = 0$ and $T = 1$ states degenerate in the low-energy region. In this section, we explain the framework of the isospin projected AMD, which is a newly developed method for the study of $N = Z = \text{odd}$ nuclei. We also describe the detailed formulation of the present calculation which is based on the isospin projected version of the $\beta\gamma$ constraint AMD combined with the GCM.

2.1 AMD framework

The AMD framework is based on a variational method. An AMD wave function is a Slater determinant of Gaussian wave packets:

$$|\Phi\rangle = \mathcal{A} |\phi_1\rangle |\phi_2\rangle \cdots |\phi_A\rangle, \quad (1)$$

where \mathcal{A} refers to the antisymmetrization operator and ϕ_i refers to the i th single-particle wave function. ϕ_i is expressed by a product of the spatial(ψ_i), spin(ξ_i), and isospin(n_i) parts

as,

$$|\phi_i\rangle = |\psi_i\rangle |\xi_i\rangle |n_i\rangle, \quad (2)$$

where

$$\langle \mathbf{r} | \psi_i \rangle = \left(\frac{2\nu}{\pi} \right)^{\frac{3}{4}} \exp \left[-\nu \left(\mathbf{r} - \frac{\mathbf{Z}_i}{\sqrt{\nu}} \right)^2 + \frac{1}{2} \mathbf{Z}_i^2 \right], \quad (3)$$

$$|\xi_i\rangle = \xi_{i\uparrow} |\uparrow\rangle + \xi_{i\downarrow} |\downarrow\rangle, \quad (4)$$

$$|n_i\rangle = |p\rangle \text{ or } |n\rangle. \quad (5)$$

The parameters of Gaussian centroids $\{\mathbf{Z}_i\}_{i=1,2,\dots,A}$ and those of spin orientations $\{\xi_i\}_{i=1,2,\dots,A}$ are optimized in the energy variation, whereas each isospin configuration is fixed to be a isospin eigenstate as $|p\rangle$ or $|n\rangle$.

In the AMD wave function expressed by a Slater determinant, some symmetries such as the parity and rotational symmetries are usually broken. To obtain physical wave functions for energy levels, the parity and angular momentum projections are performed to restore the broken symmetries in the AMD framework. In most cases, the parity projection is performed before the energy variation but the angular momentum projection is done after the variation to save computational costs except for the extended AMD calculation with the variation after the parity and angular-momentum projections (AMD+VAP^J) [20]. Namely, energy variation is performed for the AMD wave function projected on to the parity eigenstate with the parity projection operator P^π as

$$\delta \frac{\langle \Phi^\pi | H | \Phi^\pi \rangle}{\langle \Phi^\pi | \Phi^\pi \rangle} = 0, \quad (6)$$

$$|\Phi^\pi\rangle = P^\pi |\Phi\rangle. \quad (7)$$

The expectation value of an observable O is calculated by the parity and angular momentum eigenstates $|\Phi_{MK}^{\pi J}\rangle$ projected from the obtained AMD wave function as,

$$\langle O \rangle = \frac{\langle \Phi_{MK}^{\pi J} | O | \Phi_{MK}^{\pi J} \rangle}{\langle \Phi_{MK}^{\pi J} | \Phi_{MK}^{\pi J} \rangle}, \quad (8)$$

$$|\Phi_{MK}^{\pi J}\rangle = P^\pi P_{MK}^J |\Phi\rangle, \quad (9)$$

where P_{MK}^J is the angular momentum projection operator. For numerical calculation of the energy variation, we adopt the frictional cooling method, which is a gradient method.

To describe the ground and excited states, we superpose various AMD wave functions based on the GCM with the $\beta\gamma$ constraint AMD method [19], which is an efficient method to choose basis AMD wave functions for a multi-configuration calculation.

In the $\beta\gamma$ constraint AMD, the energy variation is performed under the constraint on quadrupole deformation parameters β and γ . The method has been proved to be useful to describe spatially developed cluster states as well as deformed states. To perform the energy variation with a constraint $\bar{C}[\Phi] = C_i$, we add a penalty term to the energy expectation value as,

$$\langle H \rangle \rightarrow \langle H \rangle + \eta (\bar{C}[\Phi] - C_i)^2, \quad (10)$$

where η is an enough large positive value. After the energy variation with the penalty term, we obtain the optimized configuration $\Phi(C_i)$ for the energy minimum state in the AMD model space with the condition $\bar{C}[\Phi] = C_i$.

We superpose the wave functions obtained for different constraint values C_i based on the GCM method with the generator coordinate $\bar{C}[\Phi]$. In the $\beta\gamma$ constraint AMD, C_i indicates the set of the quadrupole deformation parameters, $C_i = (\beta_i, \gamma_i)$, which specifies the nuclear deformation. Then, the GCM wave function is given by the superposition of the parity and angular momentum projected wave functions obtained by the $\beta\gamma$ constraint AMD as,

$$|\Psi\rangle = \sum_{i=1}^{i_{\max}} \sum_{K=-J}^J g_{iK}^{\pi J} P^\pi P_{MK}^J |\Phi(C_i)\rangle, \quad (11)$$

where K refers to the intrinsic magnetic quantum number and i_{\max} is the number of superposed wavefunctions. The coefficients $\{g_{iK}^{\pi J}\}$ are determined by the diagonalization of the Hamiltonian and norm matrices.

2.2 isospin projection

In $N = Z = \text{odd}$ nuclei, the isospin projection is necessary to describe different isospin states $T = 0, 1$, which degenerate in a low-energy region. As done for the parity projection, the isospin projection enables us to obtain the better wave function optimized for each isospin. The isospin projection is also important to obtain proper intrinsic spin structures because the isospin of a pn pair restricts the intrinsic spin of the pair because of the Fermi statistics of two nucleons.

The isospin projection operator is defined as

$$P_{T_M T_K}^T = \frac{2T+1}{8\pi^2} \int d\Omega D_{T_M T_K}^{T*}(\Omega) R^T(\Omega), \quad (12)$$

where $D_{T_M T_K}^T$ is the Wigner's D function and $R^T(\Omega)$ is the $SU(2)$ rotation operator in the isospin space. In the present calculation of $N = Z$ nuclei, we approximately perform the

isospin projection with the following operator,

$$P^T = 1 + \pi^T P_{pn}, \quad (13)$$

where $\pi^T = (-1)^Z, -(-1)^Z$ for $T = 0, 1$ respectively. Here P_{pn} is the operator which exchanges the isospin, proton \leftrightarrow neutron, of all nucleons in the AMD wave function:

$$P_{pn} |\Phi\rangle = \mathcal{A} |\psi_1\rangle |\xi_1\rangle |-n_1\rangle |\psi_2\rangle |\xi_2\rangle |-n_2\rangle \cdots |\psi_A\rangle |\xi_A\rangle |-n_A\rangle, \quad (14)$$

where $|-p\rangle \equiv |n\rangle$ and $|-n\rangle \equiv |p\rangle$. For a $N = Z = \text{odd}$ system having a proton and a neutron with a core nucleus, the operator P^T is a good approximation of the isospin projection operator provided that the core nucleus is an approximately $T = 0$ state.

2.3 isospin projected AMD

In the isospin projected AMD framework, the isospin projection is performed before the energy variation. In the present calculation, the method is used for the $\beta\gamma$ constraint AMD. Namely, the energy variation is performed with the β and γ constraints after the isospin and parity projections but before the angular momentum projection as

$$\delta \frac{\langle \Phi^{T\pi} | H | \Phi^{T\pi} \rangle}{\langle \Phi^{T\pi} | \Phi^{T\pi} \rangle} = 0, \quad (15)$$

$$|\Phi^{T\pi}\rangle = P^T P^\pi |\Phi\rangle, \quad (16)$$

with the penalty term as

$$\langle H \rangle \rightarrow \langle H \rangle + \eta \left[(\beta_i \cos \gamma_i - \bar{\beta} \cos \bar{\gamma})^2 + (\beta_i \sin \gamma_i - \bar{\beta} \sin \bar{\gamma})^2 \right], \quad (17)$$

where $\bar{\beta}$ and $\bar{\gamma}$ are defined as

$$\bar{\beta} \cos \bar{\gamma} = \frac{\sqrt{5\pi}}{3} \frac{2\langle z^2 \rangle - \langle x^2 \rangle - \langle y^2 \rangle}{R^2}, \quad (18)$$

$$\bar{\beta} \sin \bar{\gamma} = \sqrt{\frac{5\pi}{3}} \frac{\langle x^2 \rangle - \langle y^2 \rangle}{R^2}, \quad (19)$$

$$R^2 = \frac{5}{3} (\langle x^2 \rangle + \langle y^2 \rangle + \langle z^2 \rangle). \quad (20)$$

We call this method, the T -projected $\beta\gamma$ -constraint AMD ($T\beta\gamma$ -AMD). In this method, β and γ are the parameters which control the development of clusters including pn pairs. In the application to ^{10}B nucleus with $2\alpha + pn$ structures, γ plays a role of the parameter for spatial development of the pn pair whereas β is related to the α - α distance, as shown later.

After the energy variation, we perform the GCM calculation by superposing the projected AMD wave functions with respect to the discretized generator coordinates β_i and γ_i as,

$$|\Psi\rangle = \sum_{i=1}^{i_{\max}} \sum_{K=-J}^J g_{iK}^{T\pi J} P^T P^\pi P_{MK}^J |\Phi(\beta_i \gamma_i)\rangle. \quad (21)$$

In the present calculation, we omit the isospin mixing in the wave functions. Note that the isospin mixing by the Coulomb force can be easily taken into account in the present framework by superposing different T states in the GCM calculation.

3 Hamiltonian and parameters

The Hamiltonian used in the present work is

$$H = K - K_{\text{cm}} + V_c + V_{\text{ls}} + V_{\text{Coulomb}}, \quad (22)$$

where K , K_{cm} , V_c , V_{ls} , and V_{Coulomb} are the kinetic energy, kinetic energy of the center of mass, central force, spin-orbit force, and Coulomb force, respectively. The Coulomb force is approximated by a 7-range Gaussian as done in Ref. [21]. For the central force and the spin-orbit force, the following effective nuclear forces are adopted as done in the previous work [22]. The Volkov No.2 force [23] is used for V_c as,

$$V_c = \sum_{i<j} \sum_{k=1,2} v_k \exp \left[- \left(\frac{\mathbf{r}_i - \mathbf{r}_j}{a_k} \right)^2 \right] (W + BP_\sigma - HP_\tau - MP_\sigma P_\tau), \quad (23)$$

where $v_1 = -60.65$ MeV, $v_2 = 61.14$ MeV, $a_1 = 1.80$ fm and $a_2 = 1.01$ fm. As for the Wigner, Majorana, Bartlett, and Heisenberg parameters, we adopt the same parameters as those used in the previous work [22], $W = 1 - M = 0.40$, $M = 0.60$, and $B = H = 0.06$. These parameters reproduce the $\alpha\alpha$ scattering phase shift. Bartlett and Heisenberg parameters were fitted to the relative energy between $T = 0$ and $T = 1$ states of the ^{10}B spectra in the AMD+VAP J calculation.

For V_{ls} , the spin-orbit term of the Gaussian 3-range soft-core force (G3RS) [24, 25] is used as,

$$V_{\text{ls}} = \sum_{i<j} \sum_{k=1,2} u_k \exp \left[- \left(\frac{\mathbf{r}_i - \mathbf{r}_j}{b_k} \right)^2 \right] \frac{1 + P_\sigma}{2} \frac{1 + P_\tau}{2} \mathbf{l}_{ij} \cdot \mathbf{s}_{ij}, \quad (24)$$

$$\mathbf{l}_{ij} = (\mathbf{r}_i - \mathbf{r}_j) \times \frac{\mathbf{p}_i - \mathbf{p}_j}{2}, \quad (25)$$

$$\mathbf{s}_{ij} = \mathbf{s}_i + \mathbf{s}_j, \quad (26)$$

where $b_1 = 0.60$ fm, $b_2 = 0.447$ fm. The strengths used in the present calculation are $u_1 = -u_2 = 1300$ MeV, which were fit to reproduce the ls splitting between $3/2^-$ and $1/2^-$ states in ^9Be in the AMD+VAP J calculation [22].

4 Results

To test the applicability of the $T\beta\gamma$ -AMD, we apply it to ^{10}B and show advantages of this method. ^{10}B is an ideal benchmark nucleus for the following reasons. Firstly, ^{10}B is a $N = Z$ nucleus, in which different isospin states appear in its low-energy region. Indeed, $J^\pi T = 3^+0, 1^+0$ and 0^+1 states are known in the low-lying ^{10}B spectra. In second, ^{10}B is considered to have the $2\alpha + pn$ structure. It means that ^{10}B can be a good example of a system having a pn pair around a deformed core. We investigate structures of low-lying $T = 0$ and $T = 1$ states in ^{10}B while focusing on the pn correlation around the 2α core.

4.1 Energy variation with and without the isospin projection

In the framework of the isospin projected AMD, we obtain the state optimized for each isospin $T = 0, 1$ because the energy variation is performed for the isospin projected AMD wave function as explained previously. The variation after the isospin projection (VAP^T) is essential to clarify the nuclear structure along the $N = Z$ line on the nuclear chart because different isospin states have almost same energy and compete each other in $N = Z = \text{odd}$ nuclei. This is an advantage of the $T\beta\gamma$ -AMD superior to the usual $\beta\gamma$ -AMD, in which the variation is performed without the isospin projection. In this subsection, we compare the energy surface on the $\beta\gamma$ plane obtained by the $T\beta\gamma$ -AMD with that of the $\beta\gamma$ -AMD and show the availability of the variation after the isospin projection in the present framework, $T\beta\gamma$ -AMD.

First, we show the energy on the $\beta\gamma$ plane obtained by the $T\beta\gamma$ -AMD. Figure 1 shows the $T = 0, 1$ $\pi = +$ energy surfaces of ^{10}B obtained by the variation after the parity and isospin projections. The minimum point in the $T = 1$ plane (Fig. 1(b)) is located at $(\beta \cos \gamma, \beta \sin \gamma) = (0.4, 0.1)$ and that in the $T = 0$ plane (Fig. 1(a)) is at $(0.38, 0)$. The finite γ value is mainly caused by spatial development of the pn pair as discussed later.

Next, we discuss the results obtained by the $\beta\gamma$ -AMD, which is a conventional AMD method with the parity projection without the isospin projection. Figure 2(a) shows the $\pi = +$ energy surface of ^{10}B obtained by the $\beta\gamma$ -AMD. It is notable that there is a gap along the line from $(0.2, 0.1)$ to $(0.6, 0)$. This is caused by the drastic change of the intrinsic structure from the small γ region to the relatively large γ region.

We also calculate the energy expectation values of the $T = 0, 1$ eigenstates projected from the $\beta\gamma$ -AMD wave functions obtained by the variation before the isospin projection (VBP^T). The $T = 0$ and $T = 1$ $\pi = +$ energy surfaces of the VBP^T are shown in Figs. 2(b) and (c), respectively. Also the $T = 0, 1$ energy surfaces of the VBP^T show the discontinuity along the same line on the $\beta\gamma$ plane originating in the difference in the intrinsic structure in

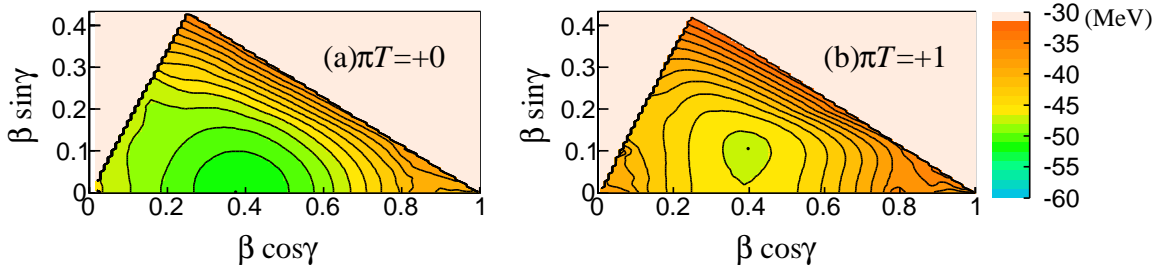


Fig. 1 Energy surfaces on the $\beta\gamma$ plane of ^{10}B obtained by the $T\beta\gamma$ -AMD. The left (right) panel shows the $T = 0(T = 1)$ $\pi = +$ energy surface. The energy minimum of each energy surface is shown by a dot.

two regions. The $T = 0$ energy surface in the small γ region corresponds well to the $T = 0$ result obtained by the VAP^T shown in Fig. 1(a), whereas the $T = 1$ energy surface in the large γ region is similar to the $T = 1$ result of the VAP^T in Fig. 1(b). This means that, for the small γ region, the VBP^T gives the wave functions almost same as those optimized for the $T = 0$ component, and for the large γ region, it produces the solutions similar to those optimized for the $T = 1$ component.

From these results, it is clear that the VBP^T method is not applicable to obtain the optimum wave functions on the $\beta\gamma$ plane for each isospin. As seen in Fig. 2(b), the VBP^T fails to obtain the $T = 1$ states in the small γ region, that is., the $T = 1$ wave functions with prolate deformations. As already shown in Fig. 1, the $T = 0$ and $T = 1$ states exist in each point on the $\beta\gamma$ plane. However, in the VBP^T , the $T = 0$ and $T = 1$ states can not be optimized separately, but either of $T = 0, 1$ states or a mixed state of $T = 0$ and $T = 1$ components is optimized. The discontinuity on the $\beta\gamma$ plane in the VBP^T results can be a crucial problem to describe the γ mode, which is related to pn pair motion, and to calculate excited states in each isospin channel.

On the other hand, the VAP^T technique enables us to optimize $T = 0$ and $T = 1$ components separately even though they almost degenerate at each constraint point. Consequently, the discontinuity on the $\beta\gamma$ plane disappears and the smooth energy surfaces are obtained for each isospin states by the $T\beta\gamma$ -AMD as shown in Fig. 1. This is one of the advantages of the present method and important to describe the γ mode for pn pair motion in detail.

4.2 Angular momentum projected energy surfaces and intrinsic structures

We discuss the angular momentum projected energies of the $T\beta\gamma$ -AMD, which are calculated by the angular momentum projection of the wave functions obtained by the $T\beta\gamma$ -AMD. Figure 3 shows the energy surfaces on the $\beta\gamma$ plane for $J^\pi T = 0^+1, 3^+0$, and 1^+0 states. Here

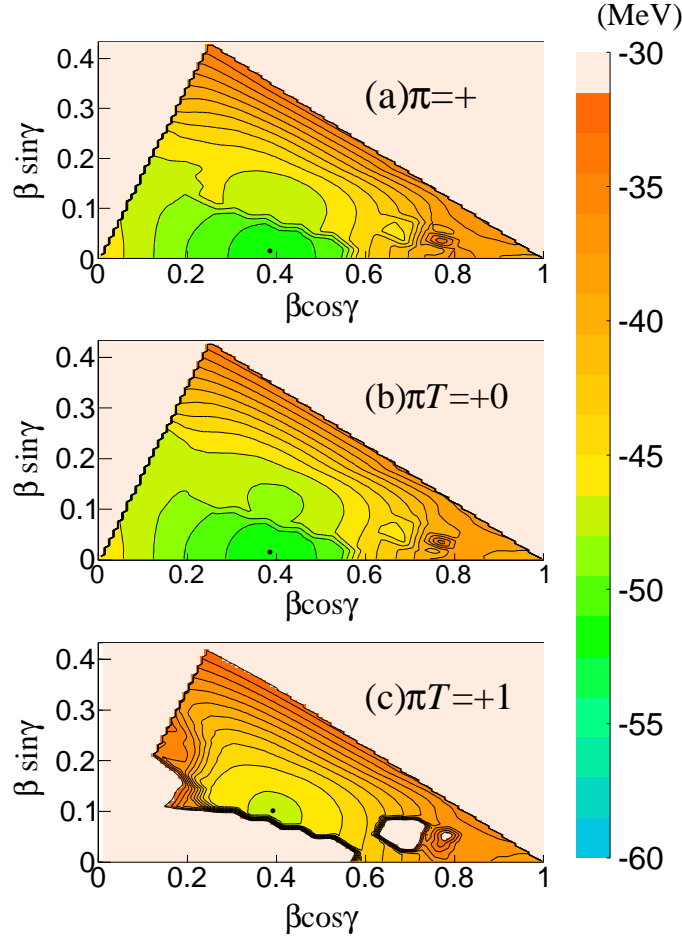


Fig. 2 Energy surfaces on the $\beta\gamma$ plane of ^{10}B obtained by the VBP^T . (a) The $\pi = +$ energy surface obtained by the $\beta\gamma$ -AMD variation without the isospin projection. (b) (c) The $T = 0$ and $T = 1$ projected $\pi = +$ energy surfaces of the VBP^T . The energy minimum of each energy surface is shown by a dot.

the K -mixing is taken into account and the lowest energy is shown at each point on the $\beta\gamma$ plane except for Fig. 3(c). The $J^\pi T = 1^+0$ states on the $\beta\gamma$ plane contain two components with different K quanta corresponding to the low-lying 1_1^+0 and 1_2^+0 states. Figures 3(b) and (c) show the energy surfaces for the first and the second lowest energies obtained by the K -mixing at each point. The 3^+0 energy surface is approximately described by the energy of the $K = 3$ component on the $\beta\gamma$ plane, whereas the 1_1^+0 and 1_2^+0 energy surfaces are roughly described by the energies of the $K = 1$ and $K = 0$ components, respectively, though strictly speaking the K -mixing occurs for $\gamma \neq 0$ states.

Compared with the $T = 0$ and $T = 1$ energy surfaces before the angular momentum projection in Fig. 1, the energy minimum positions are shifted toward larger deformation β regions by the angular momentum projection meaning that deformed states are more favored after the angular momentum projection. The energy minimum state at $(\beta \cos \gamma, \beta \sin \gamma) = (0.54, 0.12)$ for $\beta = 0.55, \gamma = 12.5^\circ$ on the $J^\pi T = 0^+1$ energy surface (Fig. 3(a)) is the dominant component of the lowest isovector ($T = 1$) state, $^{10}\text{B}(0_1^+)$, and that at $(0.52, 0.08)$ for $\beta = 0.53, \gamma = 8.7^\circ$ on the 3^+0 energy surface (Fig. 3(d)) approximately describes the lowest isoscalar ($T = 0$) state, the ^{10}B ground state (3_1^+0). The energy minimum state at $(0.5, 0.21)$ on the $J^\pi T = 1_1^+0$ energy surface and that at $(0.29, 0.27)$ on the $J^\pi T = 1_2^+0$ energy surface approximately correspond to the $^{10}\text{B}(1_1^+)$ and $^{10}\text{B}(1_2^+)$, respectively.

Let us discuss intrinsic structures of the states obtained by the $T\beta\gamma$ -AMD. The AMD wave functions before the projections at the energy minimums on the $J^\pi T = 0^+1, 3^+0, 1_1^+0$ and 1_2^+0 energy surfaces (Fig. 3(a-d)) are regarded as the intrinsic states of the dominant components of the $0^+1, 3^+0, 1_1^+0$, and 1_2^+0 states of ^{10}B . In Fig. 4, we show the intrinsic density distribution of the minimum energy states projected onto the xz plane by integrating the density along the y -axis, $\rho(x, z) = \int \rho(x, y, z) dy$. The density distribution shows the structure of a 2α core with a pn pair in the low-lying states of ^{10}B . In the 0^+1 state, three $T = 1$ pn pairs with the anti-parallel spin configuration ($S = 0$) are found in the right side forming an α cluster with a $S = 0$ pn pair nearby the α cluster. In the 3^+0 state, the $T = 0$ ($S = 1$) pn pair is formed but it shows no spatial development because the pn pair is rotating around the 2α core in the $L = 2$ (D -wave) and strongly attracted by the spin-orbit potential from the core. In the 1_1^+0 and 1_2^+0 states, a $T = 0$ pn pair has the parallel spin configuration indicating the formation of the $T = 0, S = 1$ pn pair. The pn pair in the 1^+0 states is farther away from the 2α core compared with those in the 0^+1 and 3^+0 states indicating remarkable spatial development of the $T = 0, S = 1$ pn pair.

From the analysis of intrinsic structures obtained by the $T\beta\gamma$ -AMD on the $\beta\gamma$ plane, it is found that, the $T = 0, S = 1$ ($T = 1, S = 0$) pn pair is formed in the $T = 0$ ($T = 1$) states, and it goes away in the transverse direction from the 2α with increase of γ . In other word, the γ mode on the $\beta\gamma$ plane approximately corresponds the pn pair motion relative to the 2α core.

Let us come back to the energy surfaces shown in Fig. 3. The 0^+1 energy surface shows a plateau from the minimum along the γ parameter up to the $\gamma = 60^\circ$ line, which corresponds to a soft mode of the $T = 1, S = 0$ pn pair motion relative to the 2α core in the 0_1^+1 state. The 1_1^+0 energy surface shows a more remarkable plateau for the spatial development of the $T = 0, S = 1$ pn pair. In contrast, the 3^+0 energy surface does not show such a plateau

toward the $\gamma = 60^\circ$ direction meaning that the pn pair in the 3_1^+0 state is deeply bound near the core because of the spin-orbit potential from the core.

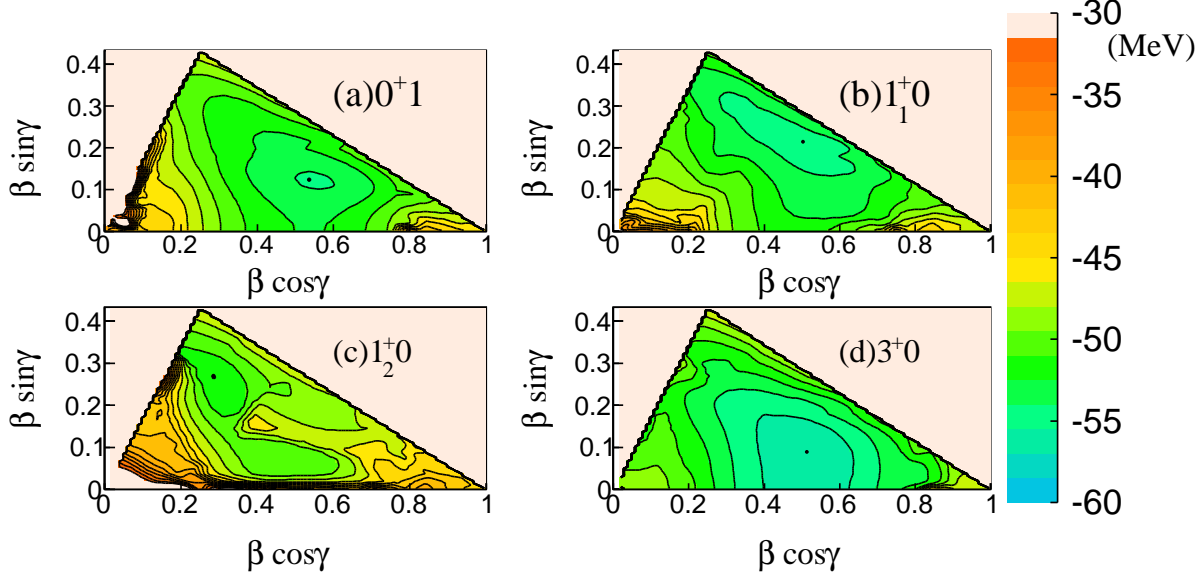


Fig. 3 J^π -projected energy surfaces of the VAP^T on the $\beta\gamma$ plane of ^{10}B . (a), (b), (c) and (d) panels refer to the 0^+1 , 1_1^+0 , 1_2^+0 and 3^+0 , respectively. The energy minimum on each energy surface is shown by a dot.

4.3 GCM results

We superpose $i_{\text{max}} = 91$ wave functions on the $\beta\gamma$ plane for each isospin and calculate energy spectra, moments, and transition strengths. The parity, isospin, and the angular momentum projections with K -mixing are taken into account in the GCM calculation as described in Eq. (21). The generator coordinates, β and γ , effectively describe the pn pair motion relative to the 2α core as well as the α - α motion.

The $T = 0$ and $T = 1$ energy spectra of ^{10}B obtained by the GCM calculation are shown in Fig. 5. Compared with the minimum energies of the $J^\pi T$ energy surfaces on the $\beta\gamma$ plane, about 4 MeV energy gain is obtained for the lowest $J^\pi T$ states by the superposition in the GCM calculation mainly because of the quantum mixing of spatial and spin configurations of the pn pair. In particular, the 1_1^+0 states gains a larger energy than the 3_1^+0 because of the spatial motion of the pn pair along the plateau on the energy surface. As a result, the excitation energy of the 1_1^+0 state decreases in the GCM calculation. Moreover, we obtain excited $J^\pi T$ states as a result of configuration mixing as well as K -mixing in the GCM calculation. The energy spectra of the GCM calculation reasonably reproduce the

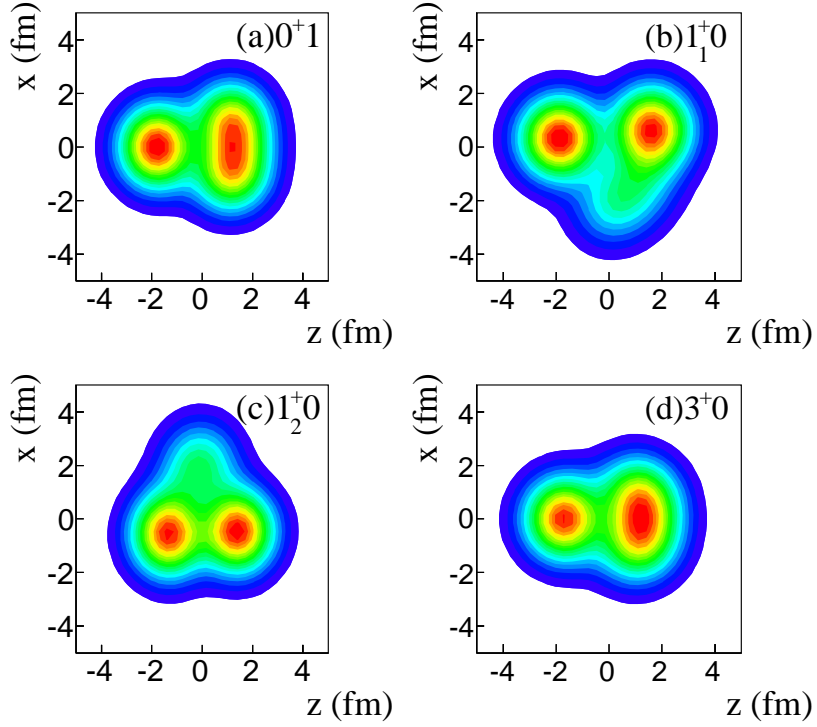


Fig. 4 Intrinsic density of the states at the minimum points in the J^π -projected energy surfaces of the VAP^T . Panels (a), (b), (c) and (d) show the density distribution projected to the xz plane of the 0^+1 , 1_1^+0 , 1_2^+0 and 3^+0 , respectively.

experimental spectra of $T = 0$ and $T = 1$ states. Note that the relative energy between the $T = 1$ states and $T = 0$ states strongly depends on the interaction parameters, B and H .

Table 1 shows the calculated values of nuclear properties compared with the experimental data. The present $T\beta\gamma$ -AMD+GCM calculation reproduces well the ground state properties such as the point-proton radius r_p , the electric quadrupole moment Q , and the magnetic moment μ , and also describes reasonably the experimental data of $E2$ and $M1$ transition strengths.

In Fig. 6, we show the overlap amplitudes of the 0^+1 , 1_1^+0 , 1_2^+0 and 3^+0 states obtained by the GCM calculation with the basis wavefunctions $\Phi(\beta_i\gamma_i)$ on the $\beta\gamma$ plane. The overlap amplitudes are calculated by the projection to the subspace composed of J^π -projected states, $\{P^T P^\pi P_{MK}^J |\Phi(\beta_i\gamma_i)\rangle\}_{K=-J,\dots,J}$. For the $^{10}\text{B}(1_1^+0)$ and $^{10}\text{B}(0_1^+)$ states, the overlaps are distributed widely along the plateaus indicating the spatial development of the $T = 0, S = 1$ and $T = 1, S = 0$ pn pairs, respectively. For the $^{10}\text{B}(3_1^+0)$, the overlap is distributed in the small γ region corresponding to the flat region around the energy minimum toward the $\gamma = 0$ line on the $J^\pi T = 3^+0$ -projected energy surface (Fig. 3 (d)). This result indicates that the

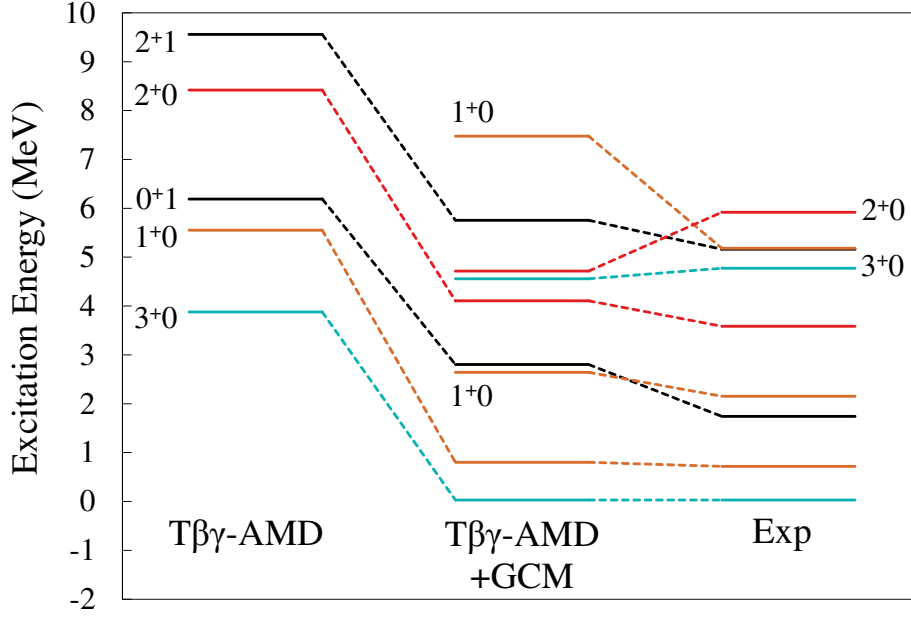


Fig. 5 Spectra of ^{10}B calculated by the $T\beta\gamma\text{-AMD}+\text{GCM}$ and those of the experimental data taken from Ref. [26]. The minimum energies in the J^π -projected energy surfaces of the $T\beta\gamma\text{-AMD}$ measured from the 3_1^+0 energy of the $T\beta\gamma\text{-AMD}+\text{GCM}$ are also shown.

$^{10}\text{B}(3_1^+0)$ has less spatial development of the pn pair and is regarded as the almost prolately deformed state with γ fluctuation.

5 Discussion

In this section, we discuss the structures of the low-lying states in ^{10}B and describe the spin and spatial configurations of the pn pair.

As discussed previously, the $T = 0$ and $T = 1$ states of ^{10}B have dominantly the $S = 1$ and $S = 0$ pn pairs around the 2α core, respectively. The finite spin ($S = 1$) of the $T = 0$ pair couples with the orbital angular momentum L to the total angular momentum J . In the $2\alpha + pn$ structures, the orbital angular momentum (L_{pn}) for the pn pair motion relative to the 2α core and that ($L_{2\alpha}$) for the 2α core rotation contribute to the total orbital angular momentum L . Table. 2 shows the expectation values $\langle L^2 \rangle$ and $\langle S^2 \rangle$ of the squared total orbital angular momentum and total spin angular momentum of the 3_1^+0 , 1_1^+0 , 1_2^+0 , and 0_1^+1 states obtained by the $T\beta\gamma\text{-AMD}+\text{GCM}$. $\langle S^2 \rangle = 2.0$ of the $T = 0$ states indicates the almost pure $S = 1$ pn pair in the 3_1^+0 , 1_1^+0 , and 1_2^+0 states, and $\langle S^2 \rangle = 0.3$ of the $T = 1$

Table 1 Nuclear properties and transition strengths of ^{10}B are shown. The calculated values obtained by the $T\beta\gamma$ -AMD+GCM and these obtained for the minimum energy states of the J^π -projected energy surfaces of the $T\beta\gamma$ -AMD in Fig. 3 are shown. The results of the AMD+VAP J calculation in Ref. [22] are also shown. The experimental proton radii are derived from the charge radii in [27]. Other experimental data are taken from [26, 28].

observable	$T\beta\gamma$ -AMD	$T\beta\gamma$ -AMD+GCM	AMD+VAP J	Exp
$r_p(3_1^+0)$ (fm)	2.3	2.4	2.33	2.28(5)
$Q(3_1^+0)$ ($e\text{ fm}^2$)	7.5	8.4	8.2	8.47(6)
$\mu(3_1^+0)$ (μ_N)	1.8	1.8	1.85	1.8006
$\mu(1_1^+0)$ (μ_N)	0.8	0.8	0.84	0.63(12)
$B(E2; 1_1^+0 \rightarrow 3_1^+0)$	3.0	4.0	3.6	4.14(2)
$B(E2; 1_1^+0 \rightarrow 1_2^+0)$		9.2	10.1	15.6(17)
$B(E2; 1_2^+0 \rightarrow 3_1^+0)$		2.0	1.3	1.7(2)
$B(E2; 1_3^+0 \rightarrow 3_1^+0)$		0.1		
$B(E2; 1_1^+0 \rightarrow 1_3^+0)$		2.8		
$B(E2; 1_2^+0 \rightarrow 1_3^+0)$		1.5		
$B(M1; 0_1^+1 \rightarrow 1_1^+0)$	8.7	15.0	14.7	7.5(32)
$B(M1; 1_2^+0 \rightarrow 0_1^+1)$		0.1	0.0	0.19(2)
$B(M1; 0_1^+1 \rightarrow 1_3^+0)$		0.0		

state means the dominant $S = 0$ component with slight mixing of the $S = 1$ component in the 0_1^+1 state. It should be commented that the present results of $\langle \mathbf{L}^2 \rangle$ and $\langle \mathbf{S}^2 \rangle$ are almost consistent with those of the no-core shell model calculation in Ref. [29], in which analysis of the LS-coupling scheme was performed for light nuclei.

Then the structures of the 0^+1 , 3^+0 , 1_1^+0 and 1_2^+0 states are understood by the $T = 0$ $S = 1$ pn pair and $T = 1$ $S = 0$ pn pair moving around the 2α core as follows. We show schematic figures of spin configurations of the pn pairs and their coupling with orbital angular momentum in Fig. 7. The 0^+1 state has the dominant $L = 0$ component with the $S = 0$ pn pair in the S -wave around the 2α core. This state is the isobaric analogue state of the ^{10}Be having a $S = 0$ nn pair around the 2α core. The 1_1^+0 state dominantly contains the $L = 0$ component with the $S = 1$ pn pair in S -wave. This state is regarded as the spin partner of the 0_1^+1 state. Because of the spin-flip transition in the pn pair from $S = 0$ to $S = 1$, it has the strong $M1$ transition from the 0_1^+1 to the 1_1^+0 , as shown in Table 1. The 1_2^+0 state appears from the excitation of the orbital angular momentum from $L = 0$ to $L = 2$ mainly

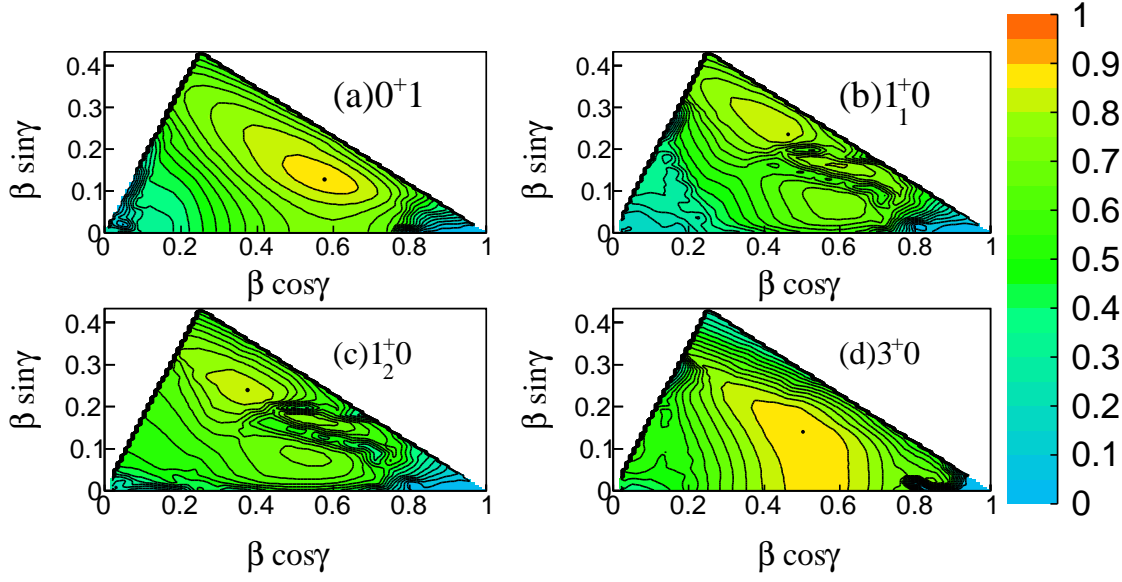


Fig. 6 Overlap amplitudes on the $\beta\gamma$ plane of ^{10}B . Panels (a), (b), (c) and (d) refer to the 0^+1 , 1_1^+0 , 1_2^+0 , and 3^+0 states, respectively. The maximum of each surface is shown by a dot.

contributed by the rotation of the 2α core ($L_{2\alpha} = 2$). The strong $E2$ transition from the 1_2^+0 state to the 1_1^+0 state (see Table 1) shows the feature of the $L_{2\alpha} = 2$ excitation in the 1_2^+0 state. The 3_1^+0 state has the dominant $L = 2$ component, which is mainly contributed by the orbital angular momentum $L_{pn} = 2$ of the $S = 0$ pn pair. From the cluster point of view, the $S = 1$ pn pair aligned to $L_{pn} = 2$ feels strong spin-orbit potential from the 2α core. The strong attraction of the spin-orbit potential for the $S = 1$ pn pair in the D -wave is the origin of the level inversion in ^{10}B between the 1_1^+0 and 3_1^+0 states with the S -wave and D -wave pn pairs, respectively as pointed out in Ref. [22]. Note that, it corresponds to the $p_{3/2}^2$ configuration in the jj -coupling scheme.

6 Summary and outlook

We developed a new framework of the isospin projected AMD with the $\beta\gamma$ constraint and the GCM called $T\beta\gamma$ -AMD+GCM for study of $N = Z = \text{odd}$ nuclei. To test the applicability of the method we applied it to ^{10}B . The formation of the $S = 1$ and $S = 0$ pn pairs around the 2α core in the low-lying $T = 0$ and $T = 1$ states of ^{10}B is described in the $T\beta\gamma$ -AMD+GCM calculation. The spatial development of the $T = 0$ and $T = 1$ pn pairs as well as the core deformation is controlled by the $\beta\gamma$ constraint in the isospin projected AMD. By

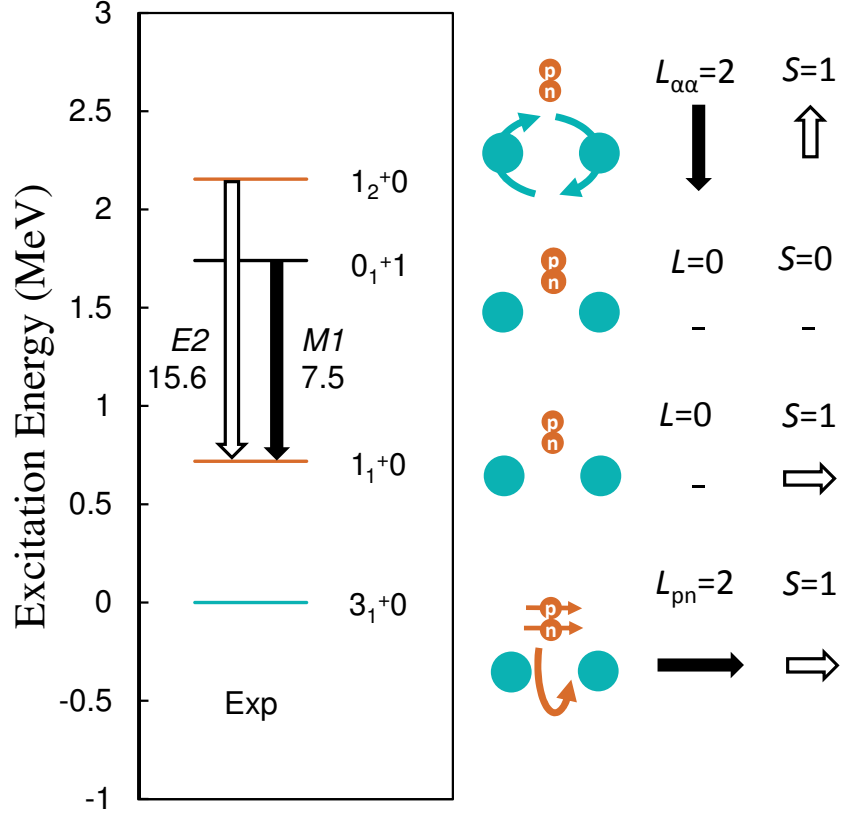


Fig. 7 The schematic figure of spin configurations of the pn pair and coupling with the orbital angular momentum in the low-lying states of ^{10}B . The experimental spectra are also shown. L , $L_{\alpha\alpha}$ and L_{pn} denote to the total orbital angular momentum, the orbital angular momentum of the 2α core and that of the center of mass motion of the pn pair. S means to the intrinsic spin of the pn pair.

superposition of the optimized wave functions on the $\beta\gamma$ plane with the GCM, the spatial motion of the pn pair as well as the core rotation is taken into account.

The $T\beta\gamma$ -AMD+GCM calculation reproduces reasonably the properties of low-lying states of ^{10}B . The structures of the lowest four states (3_1^+0 , 1_1^+0 , 1_2^+0 and 0_1^+1) are understood by the angular momentum coupling of the pn pair internal spin (S), its spatial motion, and the core rotation. The $3_1^+0(1_1^+0)$ state is described by the $2\alpha + pn$ structure having the $T = 0, S = 1$ pn pair in the D -wave(S -wave) around the 2α core. Because of the spin-orbit attraction from the core for the $S = 1$ pn pair in the D -wave, the 3_1^+0 state comes down to the ground state. The 1_2^+0 appears from the excitation of the 2α core rotation and has the strong $E2$ transition to the 1_1^+0 state. The 0_1^+1 state, which is the isobaric analogue state of

Table 2 The expectation values $\langle \mathbf{L}^2 \rangle$ and $\langle \mathbf{S}^2 \rangle$ of the squared total orbital angular momentum and total spin angular momentum. The values obtained by the $T\beta\gamma$ -AMD+GCM and those calculated for the energy minimum states of the J^π -projected energy surfaces in Fig. 3($T\beta\gamma$ -AMD).

state	$\langle \mathbf{L}^2 \rangle$		$\langle \mathbf{S}^2 \rangle$	
	$T\beta\gamma$ -AMD	$T\beta\gamma$ -AMD+GCM	$T\beta\gamma$ -AMD	$T\beta\gamma$ -AMD+GCM
3_1^+0	7.1	7.2	2.0	2.0
1_1^+0	1.0	0.4	2.0	1.9
1_2^+0		5.4		1.9
0_1^+1	0.3	0.3	0.3	0.3

the ^{10}Be ground state, is regarded as the spin partner of the 1_1^+0 state, and it has the strong $M1$ transition from the 1_1^+0 state.

It was found that the $T\beta\gamma$ -AMD+GCM can describe spin configurations and spatial development of the pn pair in $T = 0$ and $T = 1$ states as well as the core deformation and rotation. The pn pair motion relative to the core and also the shape fluctuation of the deformed core are taken into account by the $\beta\gamma$ constraint with the GCM. This is one of the advantages supplier to the AMD+VAP J which is based on the the J^π -projected wave function of a single Slater determinant. It was also shown that the isospin projection before the energy variation is necessary to obtain the optimum solution for each isospin state in $Z = N = \text{odd}$ nuclei, in which different isospin states almost degenerate in the low-energy region.

The present method is expected to be useful to investigate structure with a pn pair around a deformed core in other $N = Z = \text{odd}$ such as ^{22}Na and ^{26}Al , in which various $J^\pi T$ states appear in low-lying spectra. In principle, in the $T\beta\gamma$ -AMD+GCM, existence of a pn pair nor clusters is not *a priori* assumed. Therefore, it is applicable to general $N = Z = \text{odd}$ nuclei, and might enable us to make systematic study of pn pair correlations in nuclei along the $N = Z$ line.

Acknowledgment

The author would like to thank Dr. Kobayashi for fruitful discussions. The computational calculations of this work were performed by using the supercomputer in the Yukawa Institute

for theoretical physics, Kyoto University. This work was supported by JSPS KAKENHI Grant Number 26400270.

References

- [1] S. Frauendorf, A. O. Macchiavelli, Prog. Part. Nucl. Phys. **78** (2014).
- [2] H. Wolter, A. Faessler, P. Sauer, Nucl. Phys. **A167**, 108 (1971) .
- [3] A. L. Goodman, Adv. Nucl. Phys. **11**, 263 (1979).
- [4] A. Gezerlis, G. F. Bertsch and Y. L. Luo, Phys. Rev. Lett. **106**, 252502 (2011).
- [5] K. Yoshida, Phys. Rev. C **90**, 031303(R) (2014).
- [6] C. Qi, J. Blomqvist, T. Bäck, B. Cederwall, A. Johnson, R. J. Liotta, and R. Wyss, Phys. Rev. C **84**, 021301(R) (2011).
- [7] B. Cederwall *et al.*, Nature **469**, 68 (2011).
- [8] Y. Tanimura, H. Sagawa and K. Hagino, Prog. Theor. Exp. Phys. **2014**, 053D02 (2014).
- [9] H. Sagawa, Y. Tanimura and K. Hagino, Phys. Rev. C **87**, 034310 (2013).
- [10] Y. Fujita *et al.*, Phys. Rev. C **91**, 064316 (2015).
- [11] P. Navtáril and W. E. Ormand, Phys. Rev. C **68**, 034305 (2003).
- [12] P. Navtáril, V. G. Gueorguiev, J. P. Vary, W. E. Ormand, and A. Nogga, Phys. Rev. Lett. **99**, 042501 (2007).
- [13] A. Ono, H. Horiuchi, T. Maruyama and A. Onishi, Phys. Rev. Lett. **68**, 2898 (1992).
- [14] Y. Kanada-En'yo, H. Horiuchi and A. Ono, Phys. Rev. C **52**, 628 (1995).
- [15] Y. Kanada-En'yo and H. Horiuchi, Prog. Theor. Phys. Suppl. **142**, 205 (2001).
- [16] Y. Kanada-En'yo M. Kimura and H. Horiuchi, C. R. Physique **4**, 497 (2003).
- [17] Y. Kanada-En'yo, M. Kimura and A. Ono, Prog. Theor. Exp. Phys. **2012** 01A202 (2012).
- [18] M. Kimura, Phys. Rev. C **69**, 044319 (2004).
- [19] T. Suhara and Y. Kanada-En'yo, Prog. Theor. Phys. **123**, 303 (2010).
- [20] Y. Kanada-En'yo, Phys. Rev. Lett. **81**, 5291 (1998).
- [21] A. Ono, H. Horiuchi, T. Maruyama, A. Ohnishi, Prog. Theor. Phys. **87**, 1185 (1992).
- [22] Y. Kanada-En'yo, H. Morita and F. Kobayashi, Phys. Rev. C **91**, 054323 (2015).
- [23] A. B. Volkov, Nucl. Phys. **74**, 33 (1965).
- [24] N. Yamaguchi, T. Kasahara, S. Nagata and Y. Akaishi, Prog. Theor. Phys. **62**, 1018 (1979).
- [25] R. Tamagaki, *ibid.* **39**, 91 (1968).
- [26] D. R. Tilley, J. H. Kelley, J. L. Godwin, D. J. Millener, J. E. Purcell, C. G. Sheu, and H. R. Weller, Nucl. Phys. A **745**, 155 (2004).
- [27] I. Angeli and K. P. Marinova, At. Data Nucl. Data Tables **99**, 69 (2013).
- [28] F. Ajzenberg-Selove, Nucl. Phys. A **490**, 1 (1988).
- [29] C. W. Johnson, Phys. Rev. C **91**, 034313 (2015).